aerospace

MDPI

Communication

Maximum-Thrust Nozzle Based on Height Constraints

Bowen Huang, Jinglei Xu and Kaikai Yu *

College of Energy and Power Engineering, Nanjing University of Aeronautics and Astronautics, Nanjing 211106, China; huangbw@nuaa.edu.cn (B.H.); xujl@nuaa.edu.cn (J.X.)
* Correspondence: nuankaikai@126.com

Abstract: Compared to conventional aircraft, hypersonic aircraft place a greater emphasis on the integration of aircraft and engines to meet their high-performance requirements. The design challenges of the nozzle are evident in the requirement of a significant area ratio between the inlet and outlet, as well as the need for the aircraft to have a compact overall size. In this study, the height constraint is directly incorporated into the maximum-thrust nozzle design method. A new method is proposed for designing nozzles under height constraints, taking into consideration the maximum thrust theory. Initially, a mathematical deduction of the condition in which the nozzle achieves the maximum thrust under the height constraint is performed. The method of characteristics is then used to develop a nozzle design that satisfies the height constraint. Subsequently, the influence of the design parameters on the design method is studied in a parametric manner. The results show that the Mach number scale and asymmetrical factors can affect the length of the nozzle's ramp and flap, respectively. These factors greatly influence the performance of axial thrust and lift within a specific height constraint. Compared to the traditional truncation design method, the proposed method increases the thrust coefficient by 11.93% and the lift by 138.45%.

Keywords: maximum-thrust theory; MOC; height constraints; nozzle; scramjet

Citation: Huang, B.; Xu, J.; Yu, K. Maximum-Thrust Nozzle Based on Height Constraints. *Aerospace* **2023**, *10*, 976. https://doi.org/10.3390/aerospace10120976

Academic Editor: Sebastian Karl

Received: 4 October 2023
Revised: 5 November 2023
Accepted: 7 November 2023
Published: 21 November 2023

1. Introduction

A hypersonic vehicle refers to an aircraft that cruises within or across the atmosphere at a speed greater than *Ma*5. A scramjet, one of the main engine types used in hypersonic vehicles, has a simple structure, does not need to carry an oxidant, and is capable of horizontal takeoff and landing [1,2]. A scramjet consists of four parts: an inlet, an isolator, a combustor, and a nozzle. The nozzle is the main component that provides thrust and lift. Given that a hypersonic vehicle has a wide flight envelope, the nozzle performs well across a large nozzle pressure ratio (NPR) range, and the area ratio between the nozzle outlet and the inlet typically reaches 10. Researchers [3] have shown that a symmetric nozzle cannot meet these application requirements. Therefore, a nozzle with an asymmetric geometric structure has been developed. In addition, the geometry of the nozzle should be constrained due to the highly integrated characteristics and design requirements of hypersonic vehicles [4]. The height of the nozzle outlet affects the NPR at the design point, the windward drag of the aircraft, and the net thrust of the nozzle. Therefore, the nozzle height should be constrained directly.

Rao [5] derived the maximum thrust theory with the method of calculus of variations to improve the aerodynamic performance of nozzles. This method is widely used in the design of rocket engine nozzles. Lu [6] proposed a design method for an asymmetric nozzle based on the streamline tracing method and the maximum thrust theory. The results showed that, compared with a nozzle with straight walls, the stream-traced nozzle achieved a 2.7% increase in thrust and a 69.5% increase in lift. Lv [7] proposed an asymmetric nozzle design method based on the method of characteristics (MOC) under geometric constraints. The study also examined the influence of flap length on nozzle performance. Their proposed method could increase the axial thrust coefficient, lift, and pitching moment of the nozzle by

5.5%, 1098.2%, and 20.3%, respectively. Liu [8] developed a method for designing nozzles to control the wall pressure based on the MOC to prevent the wall pressure of the nozzle from dropping below the critical separation pressure. Yu [9] proposed an inverse design method for nozzles based on the maximum thrust theory and MOC. This method resulted in improvements in the thrust coefficient, lift, and pitching moment by 31.8%, 201%, and 56.6%, respectively. Subsequently, Yu [10] developed a nozzle design method based on the inverse design method. This method allows for the constraint of the absolute size and position of the inlet and outlet. Wang [11] proposed a nozzle design method based on the MOC, considering the impact of variable-specific heat and boundary layer development. He proved that adopting a variable geometry nozzle configuration is necessary to improve the off-design performance of a single expansion ramp nozzle (SERN).

A nozzle designed using the MOC usually has good aerodynamic performance. However, its length is excessively large, which hinders the integration of the aircraft and the engine. Researchers have proposed theories of minimum-length nozzles and truncated them to further shorten their length. Argrow [12] developed the minimal-length nozzle theory. However, ideal expansion nozzles designed using this method are still excessively long. Thus, the geometric constraints of thrust nozzles cannot be met. Shyne [13] proposed an improved method that enables the nozzle to meet size constraints and reduces its weight. The results showed that the truncation requirements should make a trade-off between the weight and performance loss of the nozzle. Hoffman [14] proposed a design method for a compressed truncated nozzle, which can effectively reduce the length of the nozzle. The performance difference between a compressed truncated nozzle and a Rao nozzle is only 0.04% to 0.34%. Lan [15] developed an inverse design method based on a three-dimensional characteristic line to design nozzles using different inlet shapes, such as circle, ellipse, and triangle shapes, and developed a nozzle design method based on the pressure inverse problem. Liu [16] developed an inverse design method based on the characteristic line tracing method, which can directly determine the viscous supersonic flow without the need for the boundary layer correction technique.

In the present study, a design method for a 2D SERN is proposed under height constraints. The accuracy and rationality of the CFD simulation are confirmed in Section 2. The design method for the SERN is introduced in Section 3. The design parameters are studied parametrically, and the effects of their mechanisms on nozzle geometry and performance are studied in Section 4. In Section 5, the performance of the nozzle designed using the proposed design method is compared with that of the nozzle designed using the traditional truncated design method. The comparison is conducted at both the same design and off-design points to confirm the superiority of the proposed design method.

2. Numerical Approaches

The commercial software ANSYS Fluent 2020 R2 is used to determine the flow fields and the aerodynamic performance of the nozzles. The governing equations are briefly described as follows:

$$\begin{gathered}\frac{\partial Q}{\partial t}+\frac{\partial E}{\partial x}+\frac{\partial F}{\partial y}=0\\ Q=\begin{bmatrix}\rho\\ \rho u\\ \rho v\\ \rho e\end{bmatrix},\ E=\begin{bmatrix}\rho u\\ \rho u^2+p-\tau_{xx}\\ \rho uv-\tau_{xy}\\ u(\rho e+p)-u\tau_{xx}-v\tau_{xy}\end{bmatrix},\ F=\begin{bmatrix}\rho v\\ \rho uv-\tau_{yx}\\ \rho v^2+p-\tau_{yy}\\ v(\rho e+p)-u\tau_{xy}-v\tau_{yy}\end{bmatrix}\\ \tau_{xx}=-\tfrac{2}{3}\mu(\nabla\cdot\vec{V})+2\mu\tfrac{\partial u}{\partial x},\ \tau_{yy}=-\tfrac{2}{3}\mu(\nabla\cdot\vec{V})+2\mu\tfrac{\partial v}{\partial y}\\ \tau_{xy}=\tau_{yx}=\mu(\tfrac{\partial u}{\partial y}+\tfrac{\partial v}{\partial x})\\ e=\tfrac{u^2+v^2}{2}+\tfrac{p}{\rho}\end{gathered}\tag{1}$$

where ρ, u, v, p, τ, and e represent the density, x-direction velocity component, y-direction velocity component, pressure, shearing stress, and total energy per unit mass, respectively. The inviscid flux is computed using the Roe flux-difference splitting scheme on the control

surfaces. A second-order upwind scheme is used to discretize the convective term. A central second-order difference scheme is used for discretizing viscous terms. An implicit scheme is used for time stepping. The method based on the least squares cell is used to compute the gradient. During the calculation, the mass flow through the inlet and the force on the ramp and flap are used to monitor convergence. The calculation can be considered convergent when the results of the above calculation remain constant as the number of iteration steps increases. In the numerical simulation, the boundary conditions (i.e., pressure inlet, pressure outlet, and pressure far field) are adopted.

Table 1 introduces all the Fluent boundary conditions used in the numerical simulation in this article.

Table 1. All Fluent boundary conditions used in the numerical simulation in this article.

Boundary Condition Type	Introduction
Pressure inlet	Defines the total pressure, total temperature, and static pressure at the inlet. In Section 2.1, the total pressure and static pressure are set as 8571 Pa, and the total temperature is set as 600 K.
Pressure far field	Defines the static pressure, static temperature, free-stream Mach number, and x and y flow components of the free stream, only when the density is calculated using the ideal gas law. In Section 2.1, the static pressure, static temperature, free-stream Mach number, and flow direction of the free stream are set as 1000 Pa, 300 K, 0.01, 1, and 0, respectively.
Pressure outlet	Defines the gauge pressure at the outlet. When the flow is supersonic, the pressure is solved under upstream conditions. In Section 4.3, the gauge pressure at the outlet is set as 3466.9 Pa.
Wall (ramp/flap)	In Section 2.1, the ramp and flap are set as no-slip and adiabatic.

2.1. Validation of Numerical Method

The SERN experimental model of NASA is used to verify the reliability and accuracy of the numerical simulation. The nozzle named GR3 in Reference [17] is selected. The outlet-to-inlet area ratio is 1.993, and the NPR is set to 8.571. A geometric model of the nozzle is shown in Figure 1.

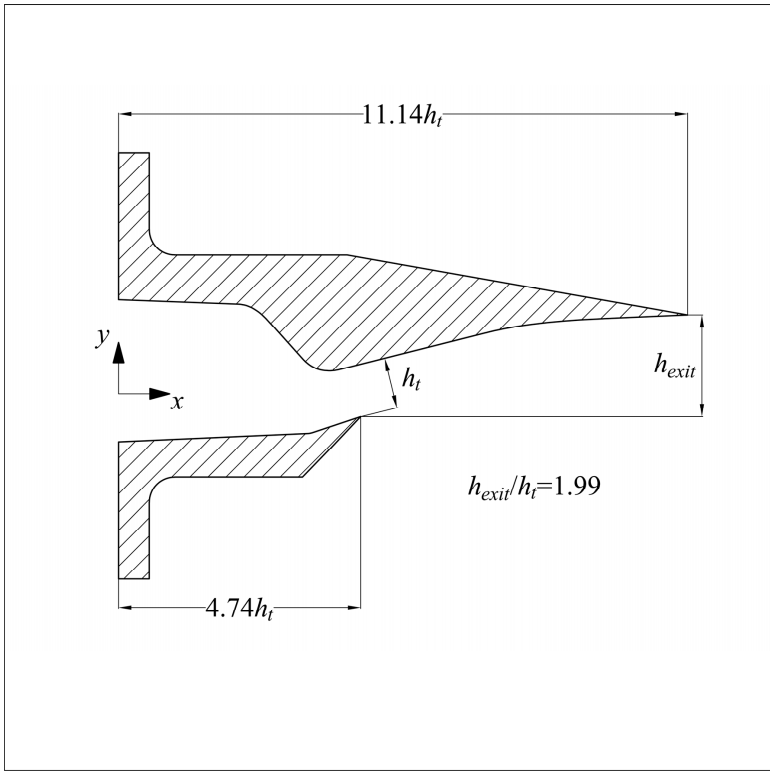

Figure 1. Sketch of the GR3 SERN.

Two turbulence models, k–ω SST and realizable k–ε, are used in the CFD simulation. The mathematical expression for the k–ω SST model is shown as (2), whereas the expression for the realizable k–ε model is shown as (3).

$$\begin{gathered}
\frac{\partial}{\partial t}(\rho k)+\frac{\partial}{\partial x_j}(\rho k u_j)=\frac{\partial}{\partial x_j}(\Gamma_k\frac{\partial k}{\partial x_j})+G_k-Y_k+G_b+S_k\\
\frac{\partial}{\partial t}(\rho \omega)+\frac{\partial}{\partial x_j}(\rho \omega u_j)=\frac{\partial}{\partial x_j}(\Gamma_k\frac{\partial \omega}{\partial x_j})+G_\omega-Y_\omega+D_\omega+G_{\omega b}+S_\omega\\
\Gamma_k=\mu+\frac{\mu_t}{\sigma_k},\ \Gamma_\omega=\mu+\frac{\mu_t}{\sigma_\omega},\ \mu_t=\frac{\rho k}{\omega}\frac{1}{\max(\frac{1}{\alpha^*},\frac{SF_2}{a_1\omega})},\\
\alpha^*=\alpha^*_\infty(\frac{\alpha^*_0+\frac{\mathrm{Re}_t}{R_k}}{1+\frac{\mathrm{Re}_t}{R_k}}),\ \mathrm{Re}_t=\frac{\rho k}{\mu\omega},\ R_k=6,\ \alpha^*_0=\frac{\beta_i}{3},\ \beta_i=0.072\\
\sigma_k=\frac{1}{\frac{F_1}{\sigma_{k,1}}+\frac{1-F_1}{\sigma_{k,2}}},\ \sigma_\omega=\frac{1}{\frac{F_1}{\sigma_{\omega,1}}+\frac{1-F_1}{\sigma_{\omega,2}}},\\
F_1=\tanh(\Phi_1{}^4),\ \Phi_1=\min[\max(\frac{\sqrt{k}}{0.09\omega y},\frac{500\mu}{\rho y^2\omega}),\frac{4\rho k}{\sigma_{\omega,2}D^+_\omega y^2}],\ D^+_\omega=\max(2\rho\frac{1}{\sigma_{\omega,2}}\frac{1}{\omega}\frac{\partial k}{\partial x_j}\frac{\partial \omega}{\partial x_j},10^{-10}),\\
F_2=\tanh(\Phi_2{}^4),\ \Phi_2=\max(\frac{2\sqrt{k}}{0.09\omega y},\frac{500\mu}{\rho y^2\omega}),\\
\sigma_{k,1}=1.176,\ \sigma_{k,2}=1,\ \sigma_{\omega,1}=2,\ \sigma_{\omega,2}=1.168,\ a_1=0.31,\ \beta_{i,1}=0.075,\ \beta_{i,2}=0.0828,\\
\alpha^*_\infty=1,\ \alpha_\infty=0.52,\ \alpha_0=\tfrac{1}{9},\ \beta^*_\infty=0.09,\ R_\beta=8,\ R_k=6,\ R_\omega=2.95,\ \zeta^*=1.5,\ M_{t0}=0.25.
\end{gathered} \tag{2}$$

$$\begin{gathered}
\frac{\partial}{\partial t}(\rho k)+\frac{\partial}{\partial x_j}(\rho k u_j)=\frac{\partial}{\partial x_j}[(\mu+\frac{\mu_t}{\sigma_k})\frac{\partial k}{\partial x_j}]+G_k+G_b-\rho\varepsilon-Y_M+S_k\\
\frac{\partial}{\partial t}(\rho \varepsilon)+\frac{\partial}{\partial x_j}(\rho \varepsilon u_j)=\frac{\partial}{\partial x_j}[(\mu+\frac{\mu_t}{\sigma_\varepsilon})\frac{\partial \varepsilon}{\partial x_j}]+\rho C_1S_\varepsilon-\rho C_2\frac{\varepsilon^2}{k+\sqrt{\nu\varepsilon}}+\frac{\varepsilon}{k}C_{1\varepsilon}C_{3\varepsilon}G_b+S_\varepsilon\\
\mu_t=\rho C_\mu\frac{k^2}{\varepsilon},\ G_k=-\rho\overline{u'_iu'_j}\frac{\partial u_j}{\partial x_i},\ G_b=-g_i\frac{\mu_t}{\rho\mathrm{Pr}_t}\frac{\partial \rho}{\partial x_i},\ Y_M=2\frac{\rho\varepsilon k}{a^2}\\
C_1=\max(0.43,\frac{\eta}{\eta+5}),\ \eta=S\frac{k}{\varepsilon},\ S=\sqrt{2S_{ij}S_{ij}},\ C_{3\varepsilon}=\tanh|\frac{v}{u}|
\end{gathered} \tag{3}$$

In (2), y is the distance to the next surface. G_k represents the generation of turbulence kinetic energy; G_ω represents the generation of ω; and Γ_k and Γ_ω represent the effective diffusivity of k and ω, respectively. Y_k and Y_ω represent the dissipation of k and ω, whereas D_ω represents the cross-diffusion term. S_k and S_ω are user-defined source terms. In

Figure 2 shows the computational grid, and Figure 3 shows a comparison of the numerical results of the normalized pressure distribution on the ramp and flap between CFD and the experiment. The numerical results show that when $x/h_t > 8$, the realizable findings of the k–ε model are closer to the experimental results than those of the k–ω SST model. Thus, all numerical simulations in the remainder of this paper use the realizable k–ε turbulence model.

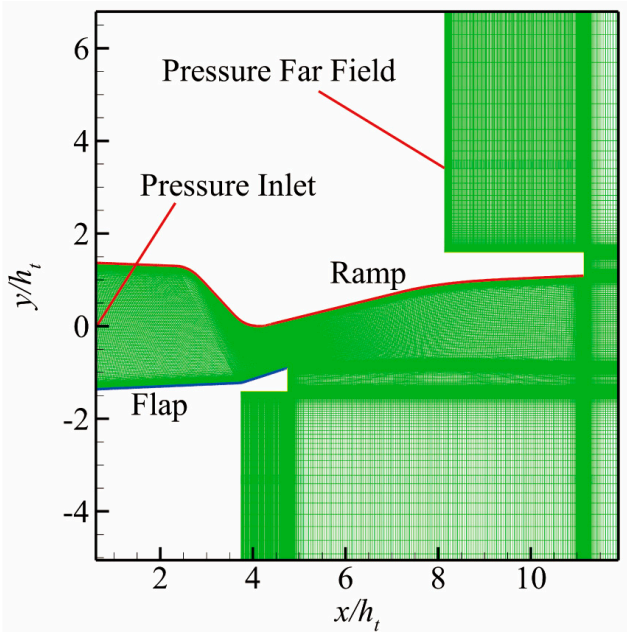

Figure 2. Computational grid of SERN.

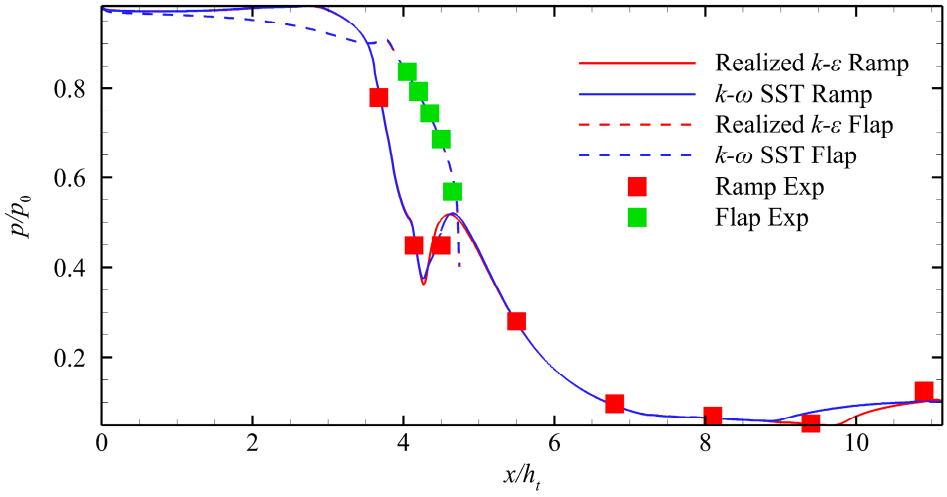

Figure 3. Comparison between CFD and experiment.

2.2. Grid Resolution Independence Study

A mesh independence study is conducted to eliminate the influence of the mesh size on the results. The computational model is the nozzle designed using the proposed method in Section 4.1, as shown in Figure 4. The computational grids of the nozzle internal flow field with different scales are used, namely, the coarse (75,000 cells), medium (150,000 cells), and fine (300,000 cells) grids. Figure 5 shows the normalized pressure distribution on the ramp using different grid scales under the same working conditions. In general, the pressure distributions obtained using the three grid sizes are the same. However, the maximum relative error between the coarse grid and the fine grid is 0.25% at $x/h_t \approx 1.8$ via amplification at $x/h_t \approx 1.8$ and 5.1. Moreover, the maximum relative error between the medium grid and the fine grid is 0.18% at $x/h_t \approx 5.1$. A medium-scale computational grid is used in the following numerical simulation to comprehensively evaluate the numerical accuracy and cost.

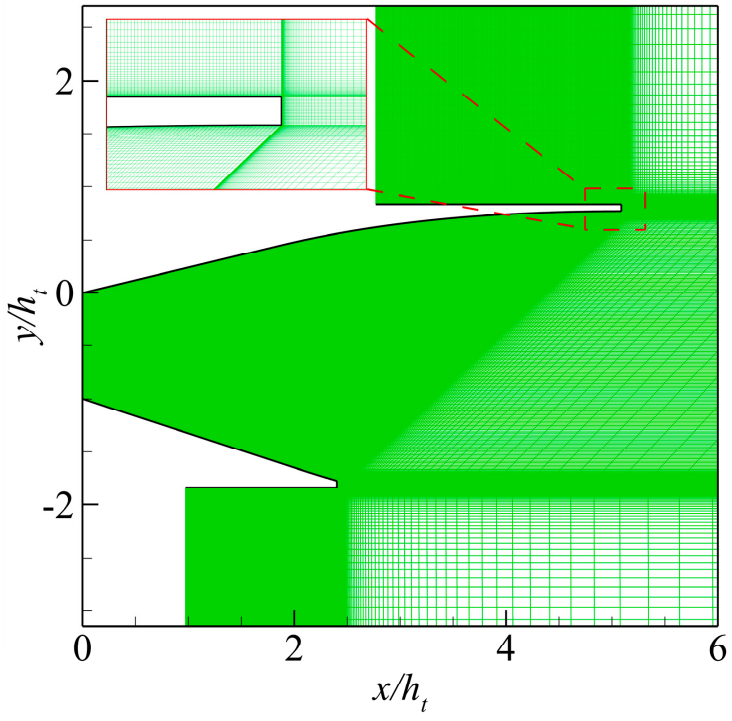

Figure 4. Computational grid of the model.

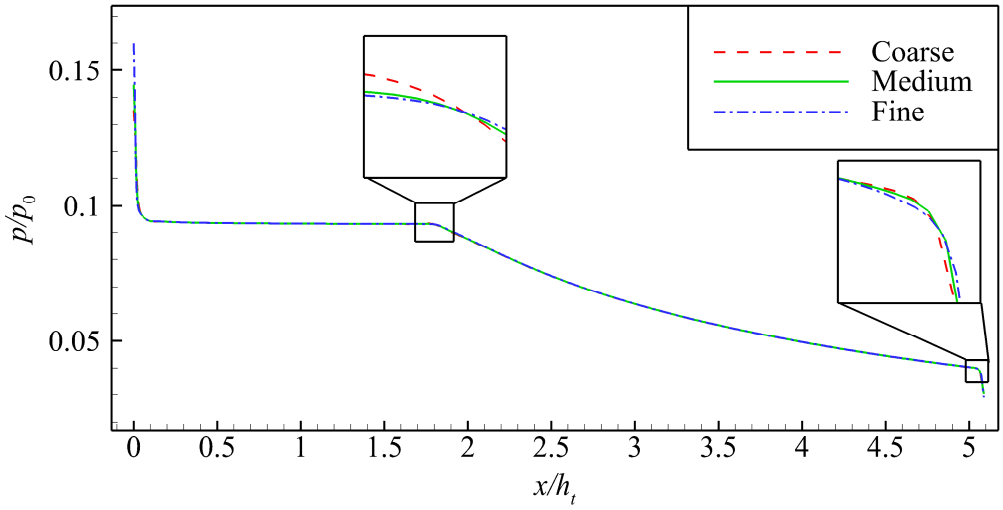

Figure 5. Influence of different grid numbers on normalized pressure distribution on the ramp of nozzle.

3. Nozzle Design Methodology

3.1. Maximum-Thrust Nozzle Theory under Height Constraint

The proposed design method draws on Rao's theory of maximum-thrust nozzles and derives the optimal design conditions of the thrust nozzle under height constraints. According to the characteristic line diagram of the maximum nozzle under the height constraint given in Figure 6, the mathematical expressions of the height constraint, h_{DE}, and the mass flow rate constraint, $\dot{m}_{DE}$, along the control surface, DE, are as follows:

$$h_{DE} = y_D + \int_D^E \tan\varphi dx \tag{4}$$

$$\dot{m}_{DE} = \int_D^E \rho V \frac{\sin(\varphi - \theta)}{\cos\varphi} dx \tag{5}$$

where θ, φ, and V refer to the velocity angle, slope angle, and velocity magnitude, respectively.

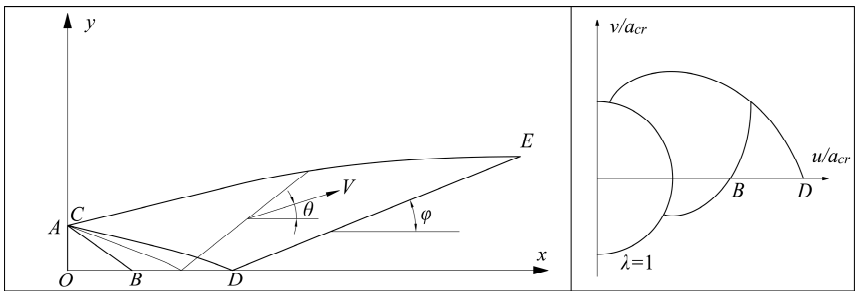

Figure 6. Schematic of characteristic lines of maximum nozzle under height constraint.

If p and p_a are the local static pressure and ambient back pressure, respectively, then the axial thrust, F, acting on the nozzle control surface, DE, is obtained as follows:

$$F = \int_D^E [(p - p_a)\tan\varphi + \rho V^2 \frac{\sin(\varphi - \theta)\cos\theta}{\cos\varphi}] dx \tag{6}$$

The Lagrangian multiplier method is applied to solve the maximum value of thrust F under flow constraint $\dot{m}$ and height constraint h. This problem is equivalent to solving the unconditional maximum value of the subsequent integral as follows:

$$I = \int_D^E f + \lambda_1 f_1 + \lambda_2 f_2 dx \tag{7}$$

where

$$f = (p - p_a)\tan\varphi + \rho V^2 \frac{\sin(\varphi - \theta)\cos\theta}{\cos\varphi} \tag{8}$$

$$f_1 = \rho V \frac{\sin(\varphi - \theta)}{\cos\varphi} \tag{9}$$

$$f_2 = \tan\varphi \tag{10}$$

The three conditions below are obtained by solving λ_1 and λ_2 as follows:

$$\varphi = \theta + \mu \tag{11}$$

$$\lambda_1 = -V \frac{\cos(\theta - \mu)}{\cos\mu} \tag{12}$$

$$\lambda_2 = -\frac{1}{2}\rho V^2 \sin 2\theta \tan\mu - p + p_a \tag{13}$$

where

$$\mu = \arcsin\frac{1}{Ma} \tag{14}$$

The corner condition is satisfied by substituting (9)–(11) into (5) as follows:

$$\sin\theta = 0 \tag{15}$$

Therefore, the axial thrust is maximum when the airflow direction is along the axial direction on the entire last characteristic line. Moreover, the aerodynamic parameters are uniformly distributed on the last characteristic line when the axial thrust is the maximum.

3.2. MOC

The governing equations of the steady supersonic flow field are hyperbolic; thus, they can be solved using the MOC. The MOC is used to calculate the steady, 2D, planar, irrotational, and supersonic flows. The characteristic line equations along the left/right running characteristic line (C_+/C_-) and their corresponding compatibility equations are as follows:

$$\frac{dy}{dx} = \tan(\theta \pm \mu) \tag{16}$$

$$\frac{\sqrt{Ma^2 - 1}}{\rho V^2} dp_\pm \pm d\theta_\pm + \delta \frac{\sin\theta}{yMa\cos(\theta \pm \mu)} dx_\pm = 0 \tag{17}$$

In the compatibility equation, $\delta = 0$ is a 2D flow, and $\delta = 1$ is an axisymmetric flow. The subscript "+" indicates the left-running characteristic line, and the subscript "−" indicates the right-running characteristic line.

The characteristic line equation along the streamline (C_0) and its corresponding compatibility equations are as follows:

$$\frac{dy}{dx} = \tan\theta \tag{18}$$

$$\rho V dV + dp = 0 \tag{19}$$

$$dp - a^2 d\rho = 0 \tag{20}$$

where a is the speed of sound.

The detailed unit process of the MOC can be found in [18].

3.3. Design Process of SERN

The design process of the maximum-thrust nozzle satisfying the height constraint based on the MOC is as follows:

(1) The ideal Mach number of the outlet, Ma_{ideal}, can be obtained using (18) according to the geometry parameters of the inlet and outlet.

$$\frac{h_{exit}}{h_{in}} = \frac{\frac{1}{Ma_{ideal}}\left[\frac{2}{\gamma+1}\left(1+\frac{\gamma-1}{2}Ma_{ideal}{}^2\right)\right]^{\frac{\gamma+1}{2(\gamma-1)}}}{\frac{1}{Ma_{in}}\left[\frac{2}{\gamma+1}\left(1+\frac{\gamma-1}{2}Ma_{in}{}^2\right)\right]^{\frac{\gamma+1}{2(\gamma-1)}}} \tag{21}$$

where h_{exit}, h_{in}, Ma_{in}, and γ are the outlet section area, inlet section area, inlet Mach number, and heat capacity ratio, respectively.

(2) The Mach region, I_uOI_d, in Figure 7 is calculated, labeled as serial number 1.

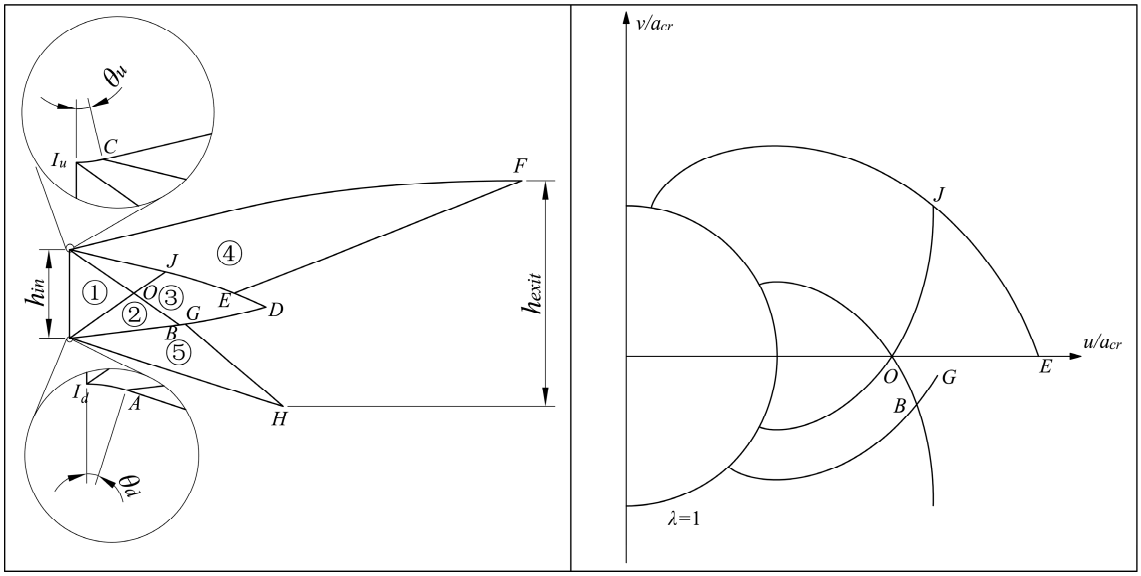

Figure 7. Schematic of MOC design procedure. ①: Mach region. ② and ③: Kernel region. ④: Upper turning region. ⑤: Lower turning region.

(3) The kernel region, I_uCDAI_dO, labeled as serial numbers 2 and 3, is calculated by considering θ_u and θ_d. Here, θ_u and θ_d represent the initial expansion angle of the ramp and flap, respectively. They are shown in Figure 7. When θ_u and θ_d are provided, asymmetrical factor β can be obtained as follows:

$$\beta = \frac{\theta_d}{\theta_u} \tag{22}$$

(4) Point E on CDA is determined, satisfying the following two conditions:

$$Ma_E = Ma_{ideal}\beta_{Ma} \tag{23}$$

$$\theta = 0^\circ \tag{24}$$

The Mach number scale factor, β_{Ma}, is a design parameter in the proposed design method. The impact of β_{Ma} on the nozzle is, therefore, examined.

If point E satisfying the conditions cannot be found, θ_u and θ_d must be provided again. Kernel region I_uCDAI_dO is calculated until the condition satisfied by point E is found.

(5) According to mass flow conservation, the last characteristic line, EF, of the upper turning region labeled as serial number 4 is determined, and the ramp profile, CF, is calculated. Section 3 shows that, if the nozzle achieves the maximum thrust while adhering to the height constraint, the last characteristic line, EF, will satisfy (20) and (21) consistently. The aerodynamic parameters on EF are evenly distributed.

(6) Point G on CDA is identified, and the last characteristic line, GH, of the lower turning region labeled as serial number 5 is determined based on mass flow conservation. The nozzle outlet, HF, meets the nozzle height constraint. The aerodynamic parameters are evenly distributed on GH.

(7) The flap profile, AH, is calculated.

The u/a_{cr}–v/a_{cr} graph is also shown in Figure 7, where λ is speed coefficient, defined as the ratio of velocity magnitude to critical speed of sound.

4. Parametric Study of Design Parameters

4.1. Typical Nozzle Design

The design performance of the proposed nozzle can be evaluated based on an actual design case. The length of the nozzle is set to 800 mm. The flight number Ma_∞ is 5.

Table 2 lists the parameters of the design condition and the geometric constraints of the nozzle required by the aircraft. The aerodynamic parameters of the nozzle inlet and the geometric constraint of the nozzle outlet height are provided. The height of the inlet (h_{in}) and outlet of the nozzle (h_{exit}) are 157 mm and 400 mm, respectively. The length of the nozzle is set to 800 mm. The flight Mach number Ma_∞ is 5. The flight altitude H is 23 km.

Table 2. Parameters of the design condition and nozzle geometric constraints.

Ma_{in}	p_{in} (Pa)	T_{in} (K)	H (km)	h_{in} (mm)	h_{exit} (mm)	L (mm)	Ma_∞
1.76	45,455	1822	23	157	400	800	5

In the design program, the initial values for θ_1, β_{Ma}, and β should be provided and are set to 30°, 1, and 0.75, respectively. A comparison of the normalized pressure contours between the inviscid CFD and MOC is shown in Figure 8. The results show the accuracy of the proposed design method.

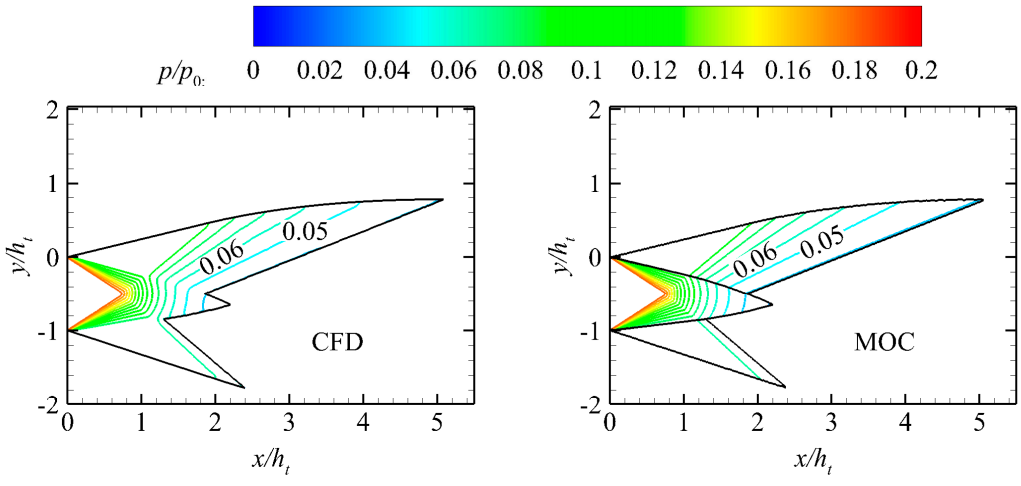

Figure 8. Pressure contours of nozzle using MOC and CFD.

4.2. Definition of Nozzle Performance Parameters

The nozzle is a key component of a scramjet, as it generates thrust, which is an important performance parameter of a scramjet nozzle. The axial thrust and lift of the nozzle are the horizontal and vertical components, respectively, of the integral of the nozzle pressure on the walls. The mathematical expressions are as follows:

$$F_x = \int_{wall} (p_w - p_a) dy \tag{25}$$

$$F_y = \int_{wall} (p_w - p_a) dx \tag{26}$$

$$F_{x,ideal} = \dot{m} \sqrt{\frac{2\gamma R}{\gamma - 1} T_0 [1 - (\frac{p_a}{p_0})^{\frac{\gamma-1}{\gamma}}]} - I_{in} \tag{27}$$

$$I_{in} = \dot{m} \overline{V}_{in} + (p_{in} - p_a) A_{in} \tag{28}$$

$$C_{fx} = \frac{F_x}{F_{x,ideal}} \tag{29}$$

$$C_L = \frac{F_y}{F_{x,ideal}} \tag{30}$$

where p_w is the wall pressure, p_a is the ambient pressure, $\dot{m}$ is the mass flow rate, T_0 is the nozzle inlet total temperature, p_0 is the nozzle inlet total pressure, $\overline{V}_{in}$ is the average axial velocity of the nozzle inlet, p_{in} is the nozzle inlet static pressure, and R is the gas constant.

4.3. Influence of β

Asymmetrical factor β primarily affects the shape of the kernel region, I_uCDAI_dO, in Figure 7, and the nozzle geometry. In the design process, θ_u remains constant when the inlet parameters, outlet height constraints, expansion arc radius, and β_{Ma} remain unchanged. The value of θ_d is determined when β is fixed.

Figure 9 shows the effect of different β values on the axial thrust coefficient and lift of the nozzle. In Figure 10, β only affects the length of the nozzle flap. However, it does not change the height of the flap or the profile of the ramp. The length of the flap decreases as β decreases, and the rate of change in the nozzle area along the axial direction increases. Thus, when β is extremely small, the separation zone appears near the flap due to the large rate of change in the nozzle area along the axial direction. The effectiveness of the design method is compromised by the separation zone. Figure 9 shows that β is positively correlated with the axial thrust coefficient C_{fx} and negatively correlated with the lift force. Figure 10 shows that the streamline near the lower wall deviates downward from the axial direction as β decreases. This phenomenon results in a decrease in axial momentum at the outlet, a decrease in axial thrust, and an increase in lift.

4.4. Influence of β_{Ma}

The Mach number scale factor, β_{Ma}, can control the overall length of the nozzle while still meeting the specified height constraint. The influence of β_{Ma} on the nozzle profile is shown in Figure 11. The figure shows that increasing β_{Ma} results in an increase in the ramp length and a decrease in the flap length. This adjustment is necessary to meet the height constraint and β.

Figure 12 shows the influence of different β_{Ma} values on the thrust coefficient and lift of the nozzle when β = 0.75. The figure shows that an increase in β_{Ma} results in an increase in the total length of the nozzle and a decrease in the length of the nozzle's flap. Thus, the positive lift provided by the ramp increases, while the negative lift provided by the flap

decreases simultaneously. The increase in the geometric asymmetry of the nozzle leads to greater inhomogeneity of the aerodynamic parameters at the nozzle outlet, resulting in a decrease in the axial thrust coefficient of the nozzle. Moreover, the calculation results show that an excessively high β_{Ma} causes significant nozzle deformation, which further leads to a severe deterioration of nozzle performance.

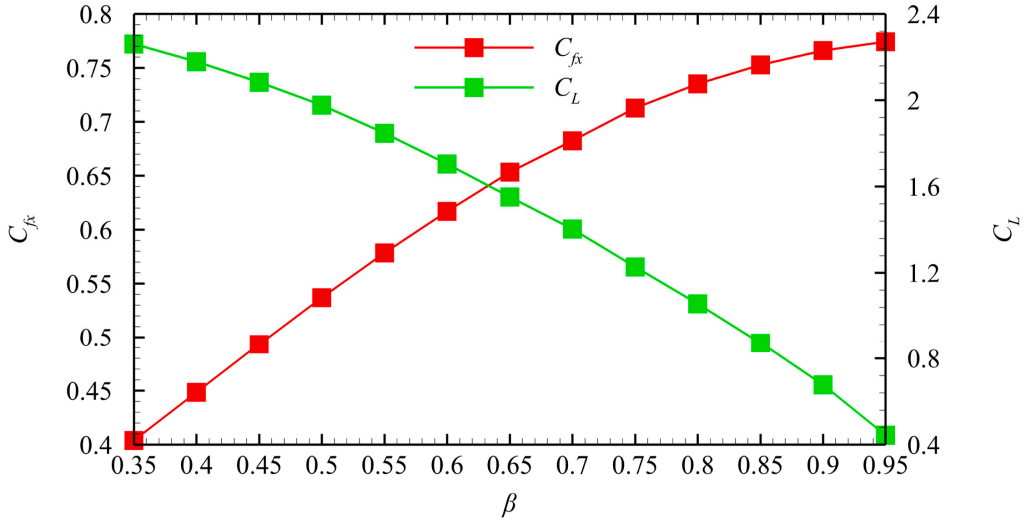

Figure 9. Thrust coefficient and lift coefficient of nozzle with different β values.

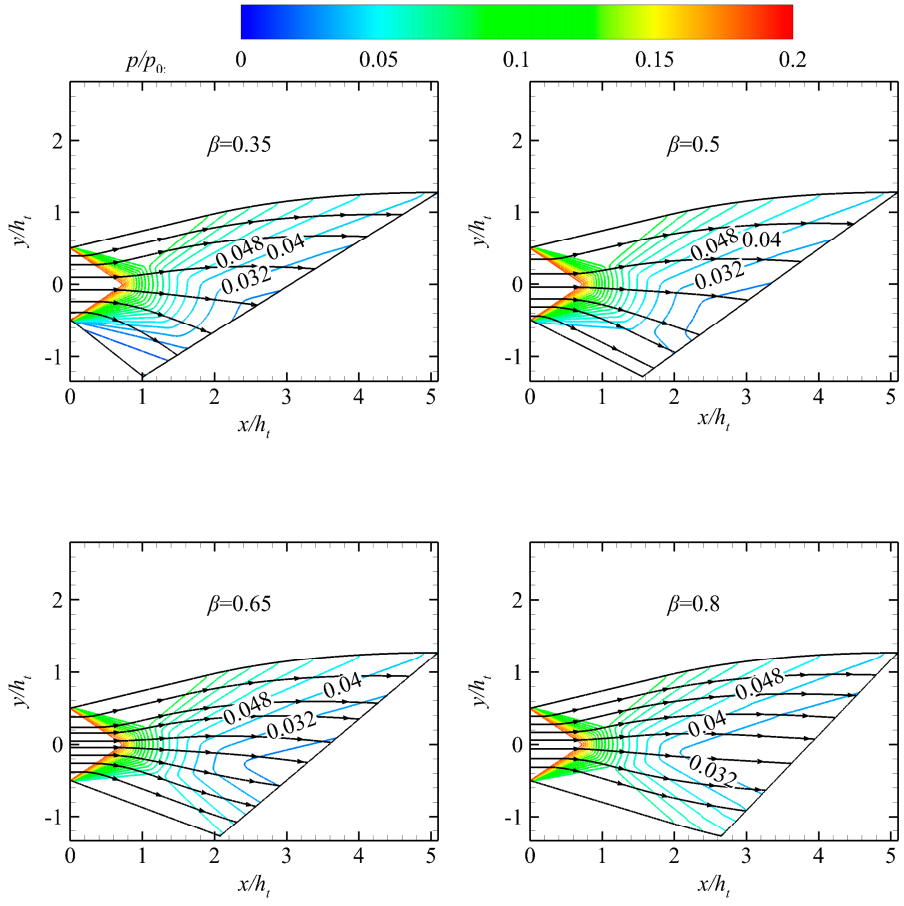

Figure 10. Pressure contours of nozzles with different β values.

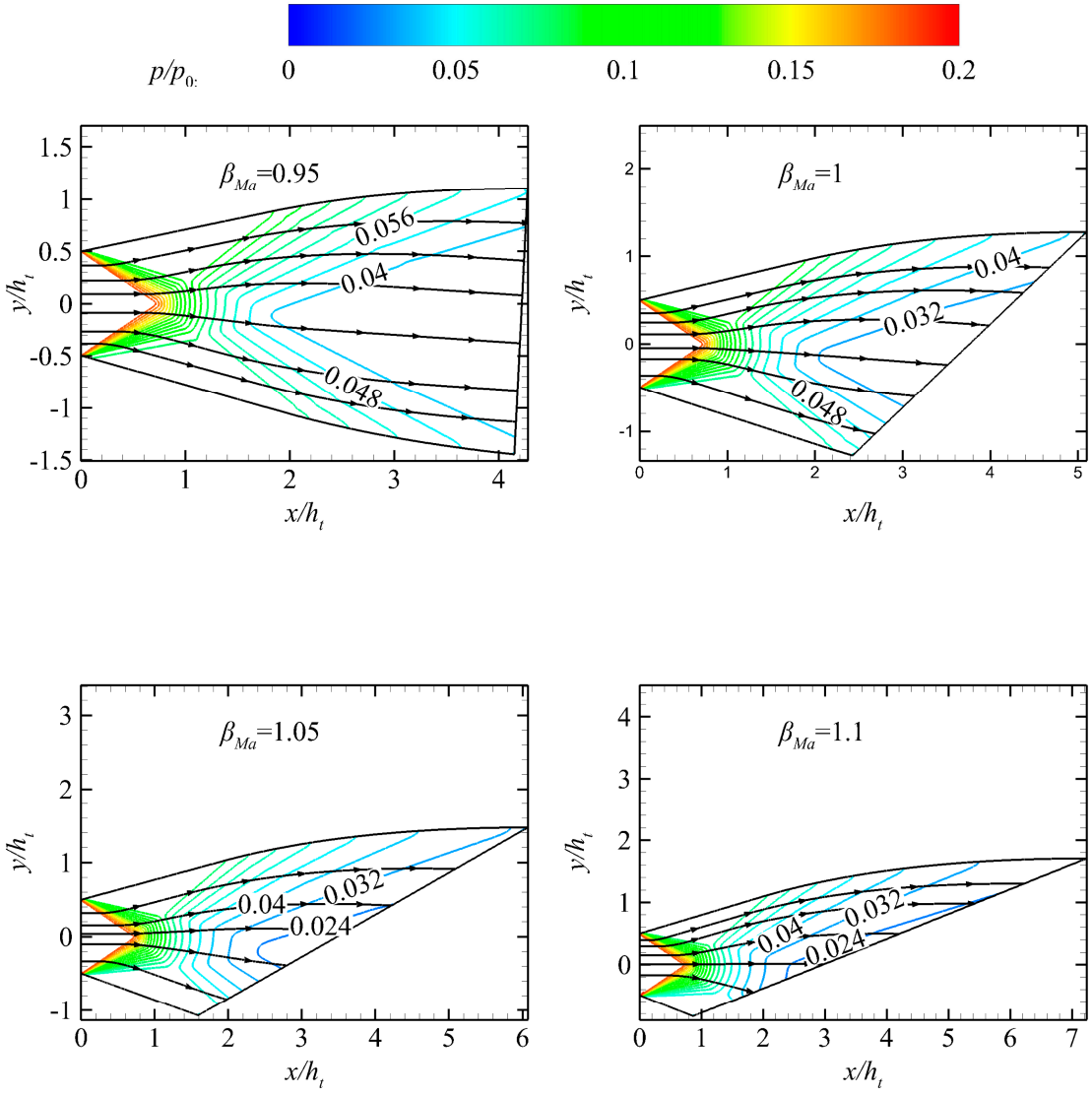

Figure 11. Pressure contours of nozzles with different β_{Ma} values.

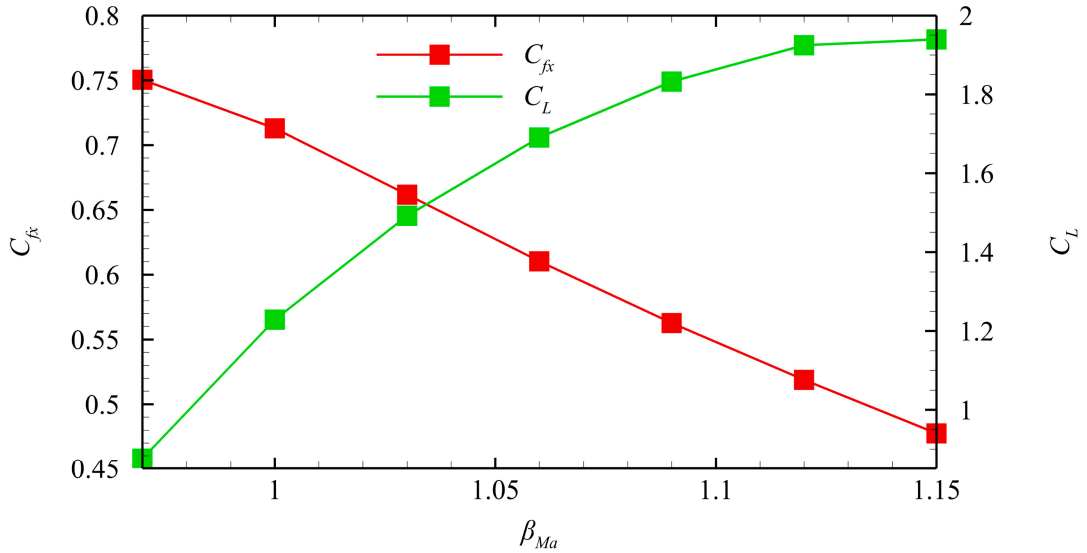

Figure 12. Thrust coefficient and lift coefficient of nozzle with different β_{Ma} values.

The influence of β_{Ma} in Figure 11 on the nozzle geometry and the nozzle design process in Figure 7 indicates that β_{Ma} can be considered a method for nozzle truncation design. When β_{Ma} is unequal to 1, the upper wall, I_uCF, is designed according to $Ma = Ma_E$ instead of $Ma = Ma_{ideal}$. Therefore, the flow design of the nozzle when β_{Ma} is larger than 1 is as follows: (1) The nozzle is designed based on the outlet Mach number Ma_E in the characteristic line design program, and the area ratio of the nozzle's inlet and outlet should conform to (18). (2) The ramp remains stationary, and the flap is truncated to meet the specified height constraint.

4.5. Adjusting Nozzle Geometry by Design Parameters

Sections 4.3 and 4.4 state that the proposed design method allows for the control of the lengths of the flap and the ramp using β and β_{Ma} while considering the given height constraint. Therefore, the two design parameters can be used to adjust the geometry of the nozzle. The influences of β and β_{Ma} on the nozzle geometry are further illustrated using three design examples.

The three sets of geometric constraints are provided by maintaining the nozzle inlet conditions and height constraints in Section 4.1, as shown in Table 3. The nozzle in Section 4.1 is referred to as Nozzle B.

Table 3. Different geometric constraints of nozzle.

Nozzle No.	Flap Length (m)	Ramp Length (m)
Nozzle C	0.8	0.3
Nozzle D	1	0.25
Nozzle E	0.7	0.4

The design process is shown in Figure 13. The design should initially be carried out according to $\beta_{Ma} = 1$. If it is not possible to meet the total length constraint, β_{Ma} should be adjusted and recalculated to ensure compliance with the constraint. Then, β_{Ma} is maintained, and β is adjusted to satisfy the constraint of the flap length.

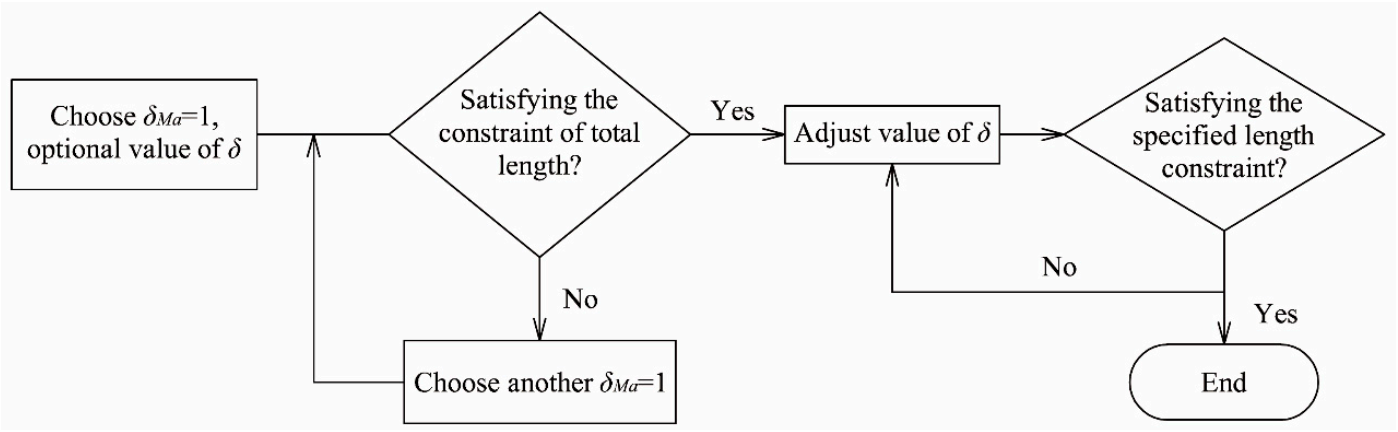

Figure 13. Design process under full geometric constraints.

The nozzles that meet the geometric constraints specified in Table 3 are designed using the design program described in Section 3.3. These nozzles also have the same height constraint as Nozzle B. The β and β_{Ma} values for each nozzle are shown in Table 4. The normalized pressure contours are shown in Figure 14, whereas the distribution of the Mach number on the outlet section is shown in Figure 15. Additionally, the pressure distribution on the ramp and flap is shown in Figure 16.

Table 4. Design parameters of different geometric constraints.

Nozzle No.	β_{Ma}	β
Nozzle C	1	0.61
Nozzle D	1.064	0.87
Nozzle E	0.963	0.625

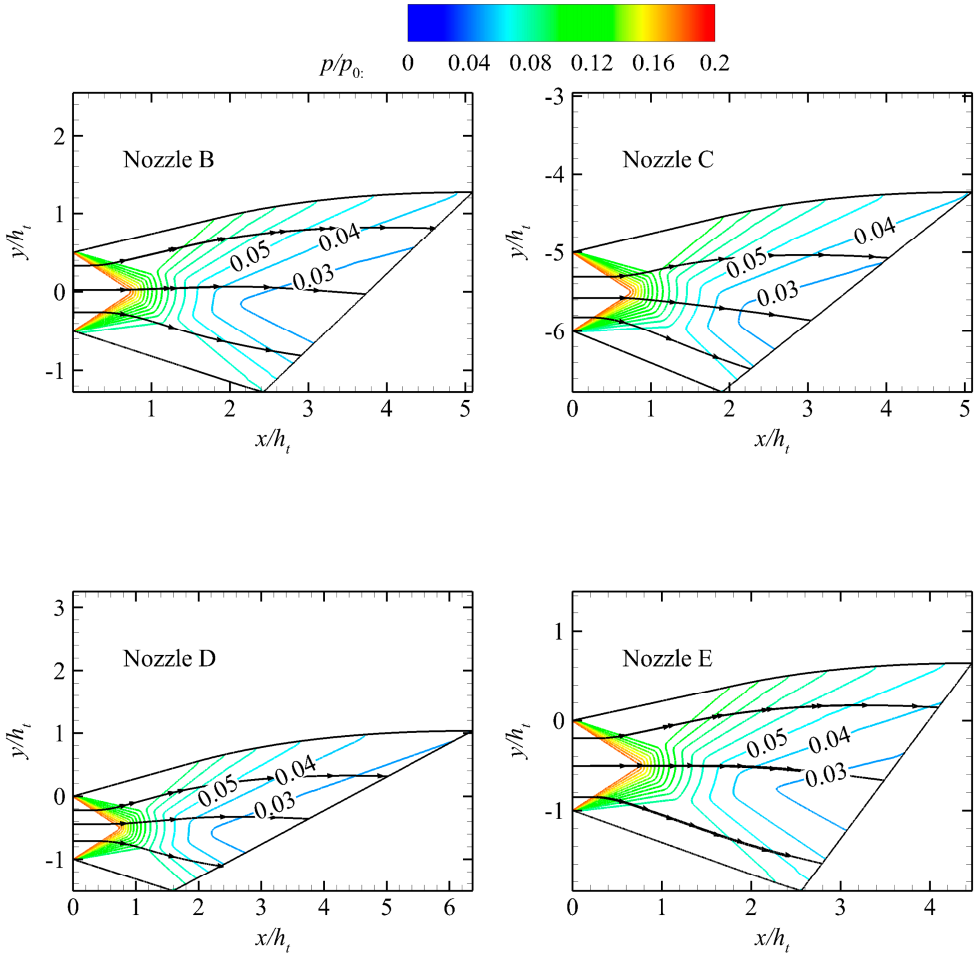

Figure 14. Pressure contours under different geometric constraints.

5. Aerodynamic Performance Comparisons Using Traditional Method

5.1. Performance Comparisons

The proposed design method is compared with the traditional truncation design method in order to prove its superiority. The typical design method is used to design a fully expanded nozzle based on the inlet and outlet conditions. The nozzle is then truncated proportionally to meet the geometric constraints. The specific design steps are shown in [19].

The nozzle designed using the truncation design method is referred to as Nozzle A. Figure 17 shows that the nonuniformity of the pressure distribution at the outlet of Nozzle A is greater than that of Nozzle B when the nozzle outlet height and nozzle inlet parameters are the same. Figure 18 shows the pressure distribution on the ramp and flap of each nozzle. Table 5 lists the axial thrust coefficient and the lift of Nozzle A and Nozzle B. The data are compared in Table 5. The results indicate that the thrust and lift coefficients are significantly improved. The lift of Nozzle B is larger than that of Nozzle A, probably because the velocity angle is equal to zero on the last characteristic line when the ramp profile is designed. Thus, the ramp of Nozzle B produces less negative lift than that of Nozzle A.

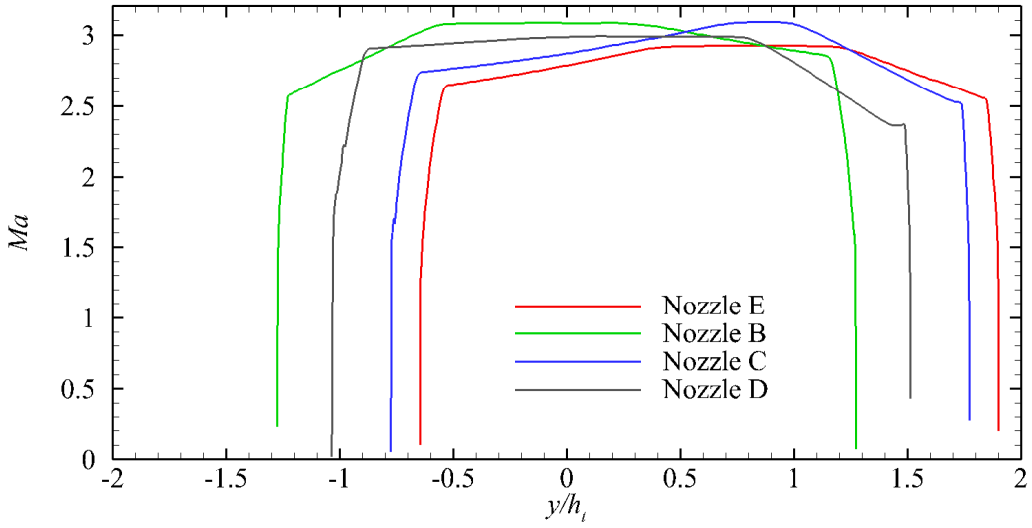

Figure 15. Mach number distribution at outlet distribution.

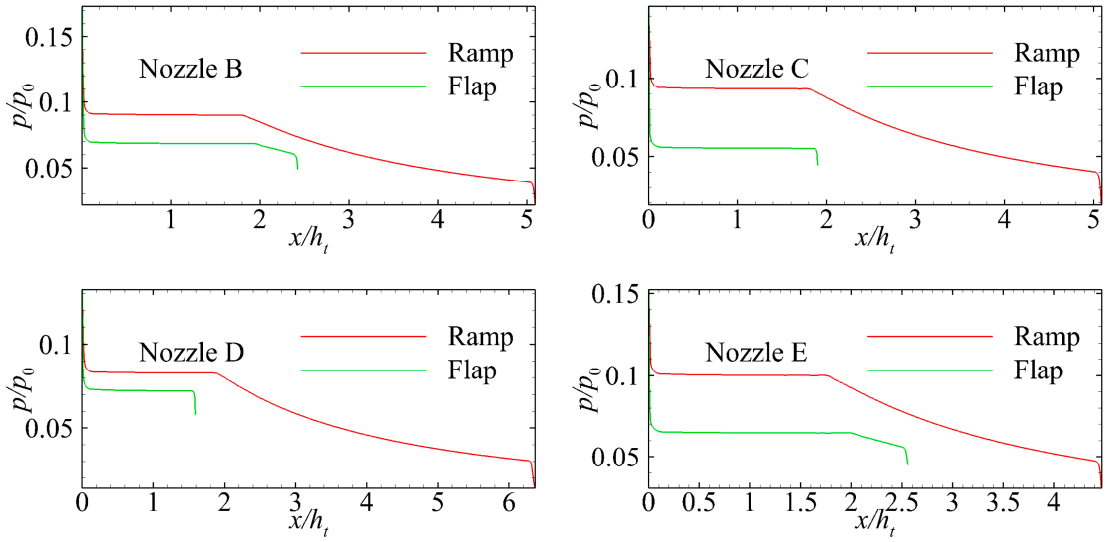

Figure 16. Pressure distribution on the ramp and flap of each nozzle.

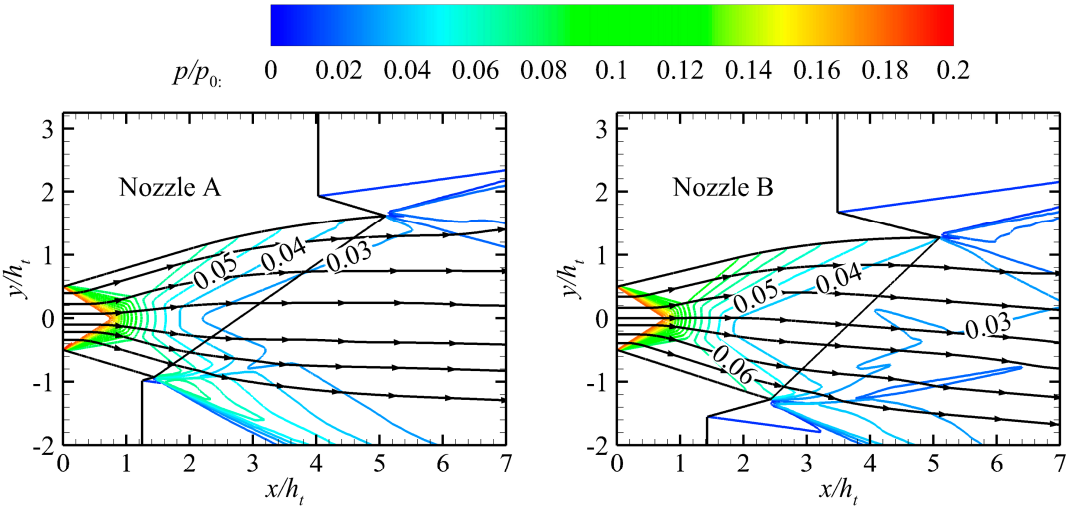

Figure 17. Comparison of pressure contours using different design methods.

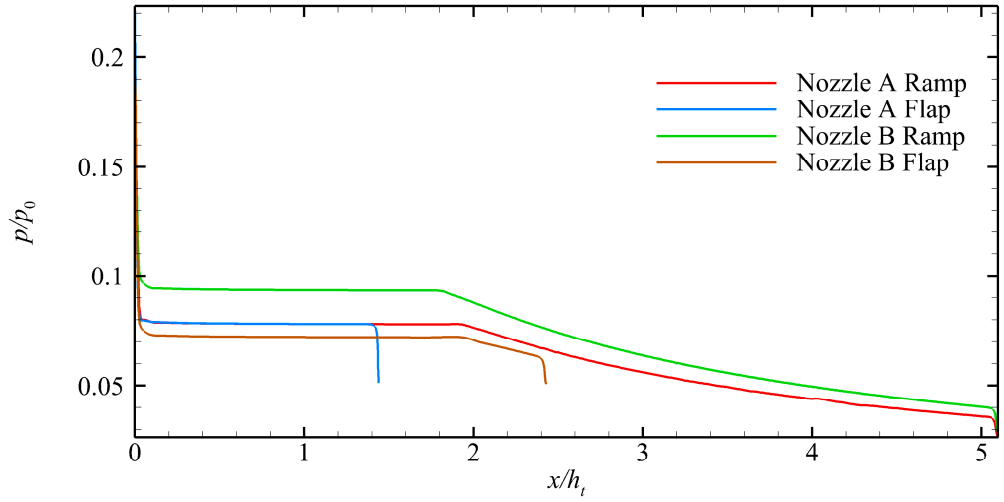

Figure 18. Wall pressure distribution of Nozzle A and Nozzle B at the design point.

Table 5. Thrust coefficient and lift coefficient using different design methods.

Nozzle No.	C_{fx}	C_L
Nozzle A	0.641	1.178
Nozzle B	0.716	1.214

5.2. Off-Design Performance

The nozzle should provide sufficient thrust when the vehicle gains altitude and takes off horizontally. Thus, the aerodynamic performance under off-design operating points should be studied. The aerodynamic performances of Nozzle A and Nozzle B are compared under off-design operating points to reflect the superiority of the proposed design method. Some typical off-design operating points are selected, as shown in Table 6. When NPR is 25.35, the nozzle is under the condition of equal expansion at the inlet and outlet sizes according to (18). At the design point, NPR is 69.22.

Table 6. Parameters of typical off-design conditions.

Ma_∞	p_a (Pa)	p_0 (Pa)	T_0 (K)	Ma_{in}
2.5	11,554.39	131,300	1500	1.37
3	8054.66	133,000	1871	1.19
3.5	5886.79	160,000	2203	1.3
4	4515.75	210,000	2409	1.4

In Table 6, the operating points Ma_∞ = 2.5 and Ma_∞ = 3 are in the overexpansion state. The operating points Ma_∞ = 3.5 and Ma_∞ = 4 are in a state of underexpansion. However, the NPR is less than that at the design point. In addition, the transition point of the combined cycle engine's working mode is typically near Ma_∞ = 2.5 during actual flight. Therefore, the off-design working points presented in Table 6 represent the typical performance of the nozzle throughout the entire flight envelope in the ramjet mode.

Figure 19 shows the normalized pressure contours for different off-design points, as listed in Table 6. Table 7 shows the thrust and lift coefficients under various off-design conditions. The aerodynamic performance of Nozzle A is also calculated under the various off-design conditions listed in Table 6. The normalized pressure contours are shown in Figure 20, and the thrust and lift coefficients are shown in Table 8. Figure 21 shows the pressure distribution on the ramp and flap of each nozzle at different operating points.

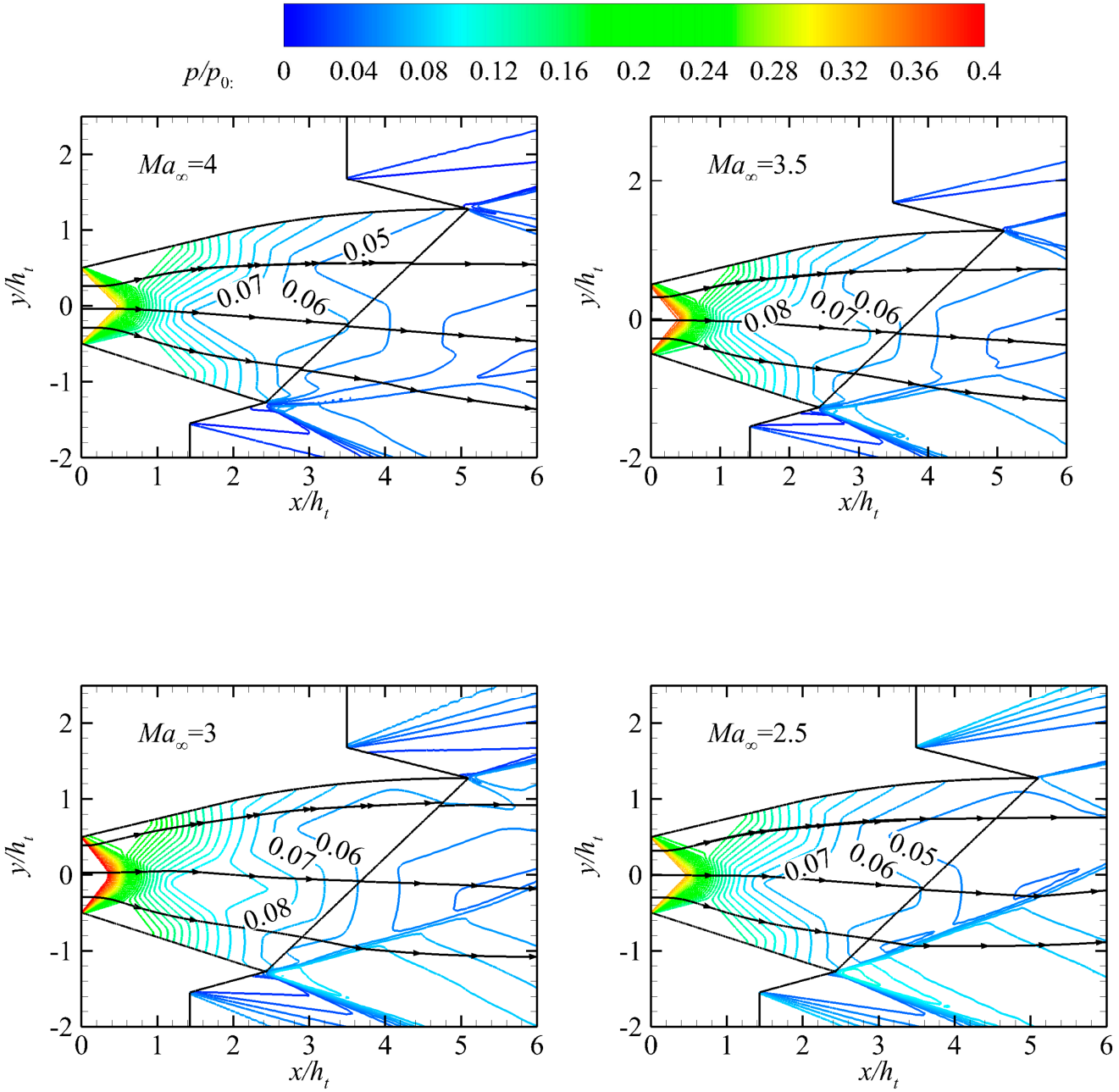

Figure 19. Normalized pressure contours of Nozzle B at different typical off-design working points.

Table 7. C_{fx} and C_L of Nozzle B at different typical off-design working points.

Ma_∞	C_{fx}	C_L
2.5	0.671	−0.007
3	0.868	0.681
3.5	0.840	0.859
4	0.767	0.908

Figure 19 shows that an increase in the NPR results in a decrease in the intensity of the oblique shock wave at the nozzle outlet. It also leads to an increase in the downward angle of the streamline near the flap outlet and causes the streamline near the ramp outlet to align more closely with the horizontal direction. The change in the streamline near the flap in Figure 20 is the same as that in Figure 19. However, the streamline near the ramp always

moves upward. The positive lift generated by Nozzle B is larger than that generated by Nozzle A under the same working conditions due to the difference in the streamline on the ramp between the two nozzles. By comparing the thrust data, it is found that the thrust coefficient of Nozzle B is slightly larger than that of Nozzle A. This finding proves that the aerodynamic performance of the nozzle is superior when using the proposed design method compared to the traditional proportional truncation method, especially under off-design conditions.

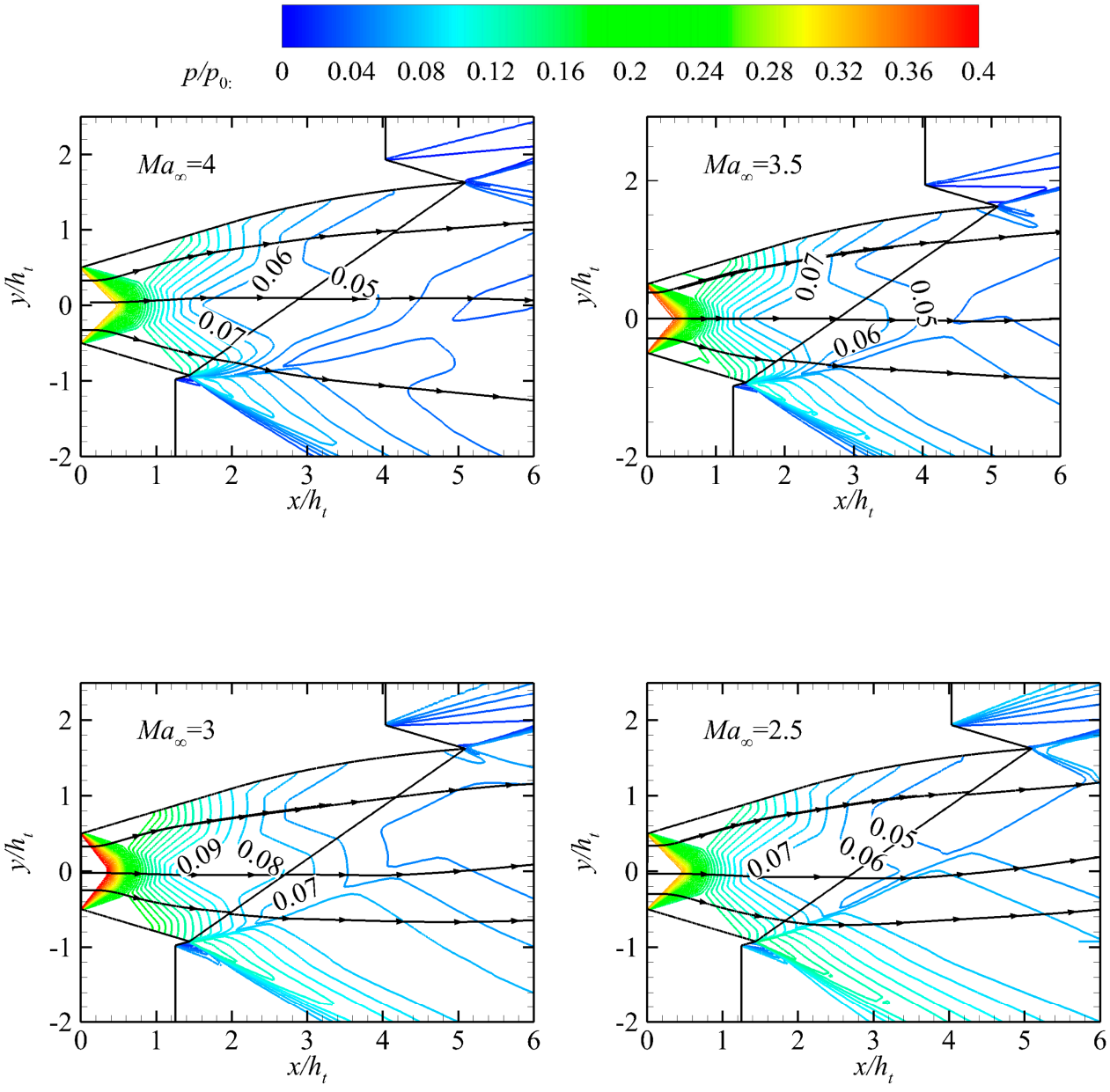

Figure 20. Normalized pressure contours of Nozzle A at different typical off-design working points.

Table 8. C_{fx} and C_L of Nozzle A at different typical off-design working points.

Ma_∞	C_{fx}	C_L
2.5	0.517	−1.010
3	0.801	0.302
3.5	0.777	0.705
4	0.708	0.866

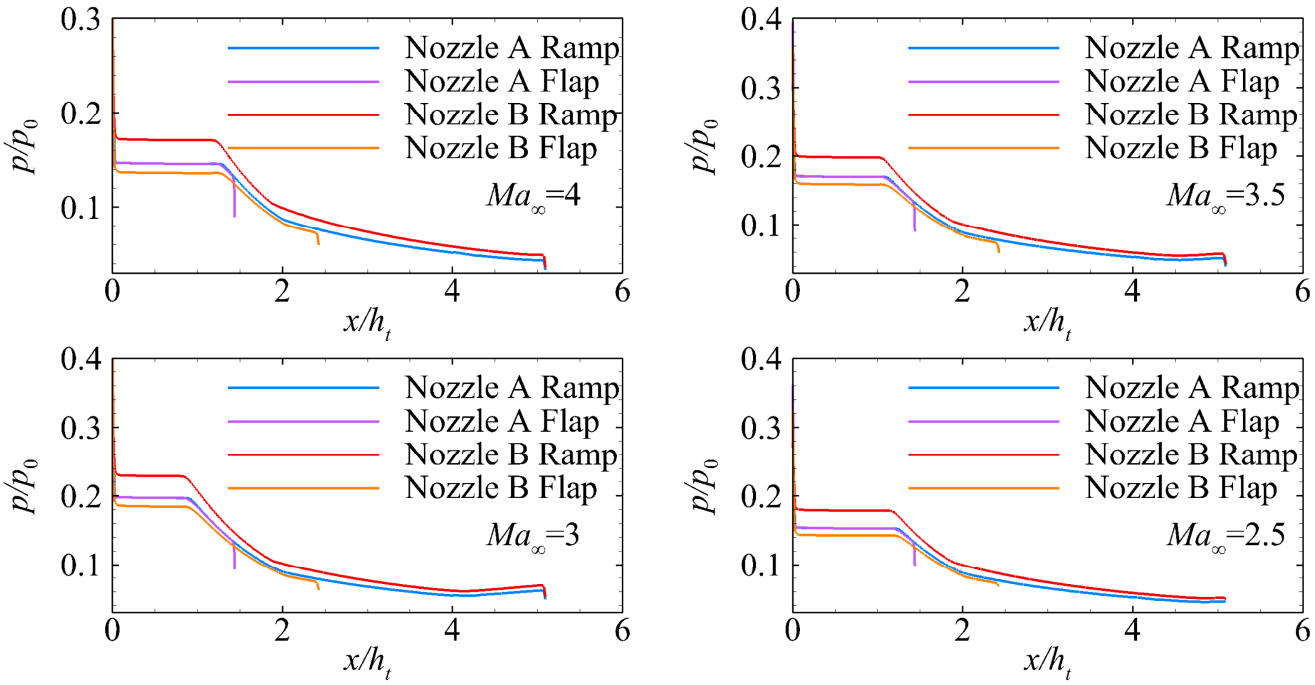

Figure 21. Pressure distribution on the ramp and flap of each nozzle at different operation points.

6. Discussion

In this design method, the flow angle on the last characteristic line of the flap is not zero. Figure 22 shows a couple of ways to design a maximum-thrust nozzle based on height constraints. The two parameters β and β_{Ma} are set as 0.75 and 1, respectively. In this figure, Method 1 is the method mentioned in Section 3.3. In Methods 2–4, the characteristic line grid is calculated sequentially to obtain the nozzle profile. Point B is calculated using the symmetric unit process. In Method 2, arc I_dD is calculated using asymmetric factor β, which leads to the last characteristic line of flap EF. The location of point F is determined via point G when the nozzle meets the height constraint. In Methods 3 and 4, the generation of the ramp profile is consistent with Method 2. The calculation of arc I_dD is also calculated using β, whereas point E is calculated using the symmetric point unit process. Then, this leads to the last characteristic line of flap EF, ensuring that the conditions of axial flow and evenly distributed parameters are met. However, the height of the nozzle exceeds the given height constraint, so truncation is necessary. To ensure that the flow at the wall outlet is horizontal, either the ramp or the flap should be truncated. Method 3 involves truncating the lower wall, while Method 4 involves truncating the upper wall, as indicated by serial number ⑥. In Method 4, the profile is not designed according to $Ma = Ma_{ideal} = f(h_{exit}/h_{in})$, that is, $\beta_{Ma} \neq 1$. Therefore, the discussion revolves around Methods 1–3.

Figure 23 shows the nozzle profiles obtained using Methods 1–3. Overall, there is not much difference in the profiles obtained using the three design methods. In theory, the denser the characteristic line grid, the greater the overlap of the profiles obtained using the three design methods. So, it can be proven that these three methods are equivalent.

Method 3 achieves the horizontal flow condition on the last characteristic line of both the ramp and flap before truncation. However, when the Mach number of point E is also calculated using $Ma = Ma_{ideal} = f(h_{exit}/h_{in})$, the nozzle meets the height constraint. At that time, the nozzle becomes a symmetric nozzle, which does not match the SERN of the research object.

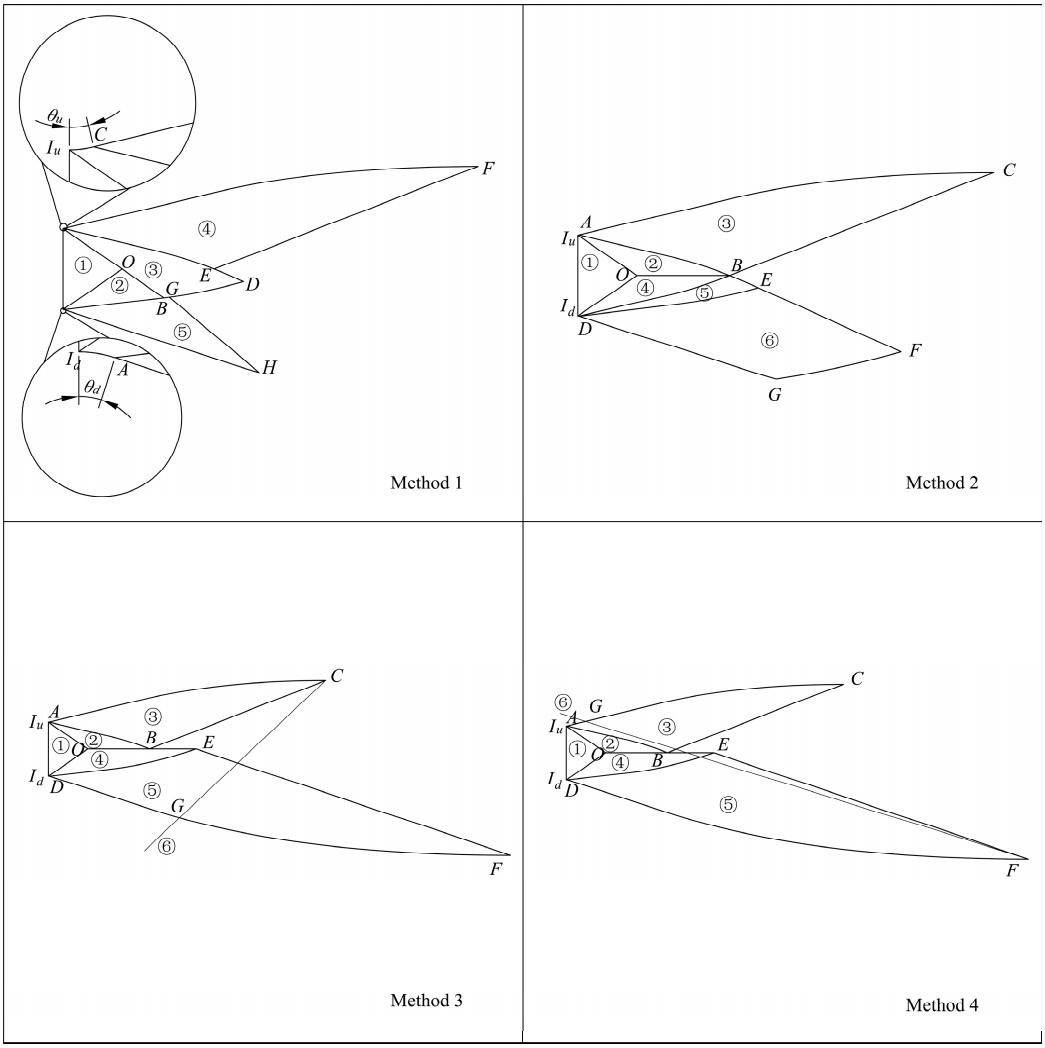

Figure 22. Several expressions of the design method for maximum thrust SERN based on height constraint. For Methods 2–4: ①: Mach region. ② and ④: Kernel region. ③: Upper turning region. ⑤: Kernel region (Method 2), lower turning region (Methods 3 and 4). ⑥: Lower turning region (Method 2), truncation (Methods 3 and 4).

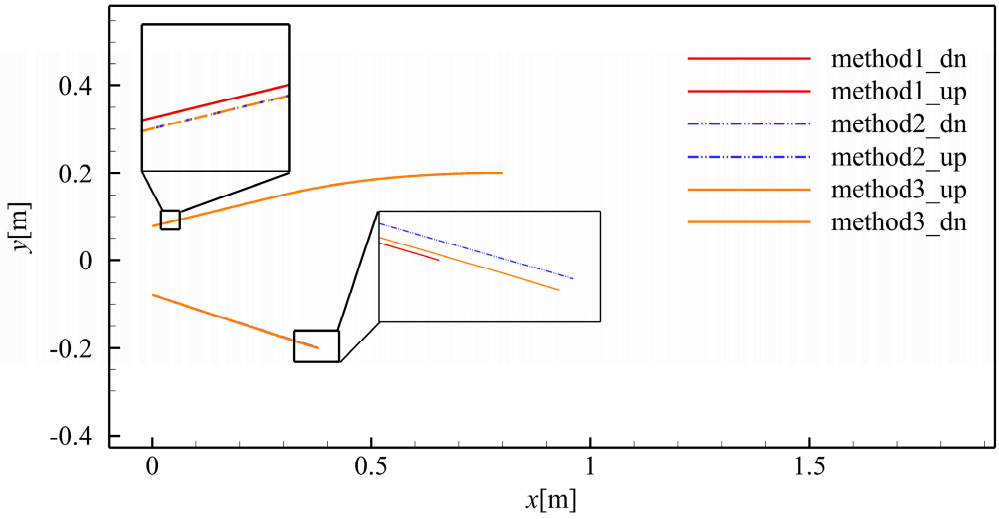

Figure 23. Comparison of nozzle profiles generated using Methods 1–3.

7. Conclusions

In this study, the height constraint is directly introduced into the maximum-thrust nozzle theory, and a maximum-thrust nozzle satisfying the height constraint is designed using the MOC. In this design method, the lengths of the nozzle's ramp and flap are controlled by adjusting β and β_{Ma} while adhering to the specified outlet height constraint. The main conclusions are as follows:

(i). β_{Ma} primarily controls the overall length of the nozzle. The total length of the nozzle increases with an increase in β_{Ma}. The length of the flap decreases, and the positive lift of the nozzle increases in order to meet the height constraint. The increase in β_{Ma} increases the geometric asymmetry of the nozzle while decreasing C_{fx} and increasing C_L. In the actual design, an excessively large β_{Ma} leads to a rapid deterioration of nozzle performance when β and the height constraint are maintained.

(ii). The influence of β on nozzle geometry is that only the length of the flap changes, while the ramp profile and the height of the flap remain unchanged. The flap length increases with an increase in β. Moreover, the streamline near the flap aligns closely with the axial direction, resulting in an increase in the thrust coefficient and a decrease in lift. In the actual design, the nozzle is designed under the specified geometric constraints by adjusting β_{Ma} and β.

(iii). Compared to the nozzle (Nozzle A) designed using the traditional truncated design method, the thrust and lift coefficients of the nozzle (Nozzle B) designed using the proposed method increase by 11.93% and 138.45%, respectively, at the design point. At the same off-design point, the thrust and lift coefficients of Nozzle B are greater than those of Nozzle A. Compared to the thrust coefficient of Nozzle A, the thrust coefficient of Nozzle B increases by a maximum of 8.79% under various typical off-design working conditions. Moreover, the positive lift force is maintained throughout the entire working condition range.

Author Contributions: Conceptualization, J.X. and K.Y.; formal analysis, K.Y. and B.H.; software, K.Y. and B.H.; validation, J.X. and K.Y.; data curation, B.H.; projection administration, J.X. and K.Y.; methodology, B.H.; supervision, J.X.; writing, B.H.; editing, K.Y.; review, J.X. All authors have read and agreed to the published version of the manuscript.

Funding: This research was funded by National Natural Science Foundation of China, grant number No. 12332018 and Postgraduate Research & Practice Innovation Program of NUAA, grant number xcxjh20220204. The authors would like to acknowledge this support gratefully.

Data Availability Statement: The data are not public due to privacy issues. The data presented in this study are available on request from the corresponding author.

Conflicts of Interest: The authors declare no conflict of interest.

Nomenclature

a	speed of sound
C_{fx}	axial thrust coefficient
C_L	lift coefficient
e	total energy
F	force
h	height
k	turbulent kinetic energy
L	length
Ma	Mach number
$\dot{m}$	mass flow rate
p	pressure
Q	rate of volumetric heat addition per unit mass
R	gas constant
T	temperature

V	velocity
x	x-direction coordinate
y	y-direction coordinate
δ	axial/2D switch
ε	kinetic energy dissipation rate
φ	slope angle
γ	heat capacity ratio
ρ	density
θ	velocity angle
τ	shearing stress
ω	specific dissipation rate
Subscript	
a	atmosphere
cr	critical parameter
$exit$	nozzle exit
in	nozzle entrance
t	throat
w	wall
0	total parameter
∞	free stream

References

1. Wang, Z.; Liang, J.; Ding, M.; Fan, X.; Wu, J.; Lin, Z. A review on hypersonic airbreathing propulsion system. *Adv. Mech.* **2009**, *39*, 716–739.
2. Wu, Y.; He, Y.; He, W.; Le, J. Progress in airframe-propulsion integration technology of air-breathing hypersonic vehicle. *Acta Aeronaut. Astronaut. Sin.* **2015**, *36*, 245–260.
3. Jin, J.; Chen, M.; Liu, Y.; Du, G. *Turbine Based Combined Cycle Engine*; National Defense Industry Press: Beijing, China, 2019; pp. 154–196.
4. Chen, Y.; Yu, K.; Xu, J. New design method for scramjet nozzles with strong geometric constraints. *Acta Aeronaut. Astronaut. Sin.* **2021**, *42*, 12459.
5. Rao, G.V.R. Exhaust nozzle contour for optimum thrust. *Jet Propuls.* **1958**, *28*, 377–382. [CrossRef]
6. Lu, X.; Yue, L.; Xiao, Y.; Chen, L.; Chang, X. Design of Scramjet Nozzle Employing Streamline Tracing Technique. In Proceedings of the 16th AIAA/DLR/DGLR International Space Planes and Hypersonic Systems and Technologies Conference, Bremen, Germany, 19–22 October 2009.
7. Lv, Z.; Xu, J.; Yu, Y.; Mo, J. A new design method of single expansion ramp nozzles under geometric constraints for scramjets. *Aerosp. Sci. Technol.* **2017**, *66*, 129–139. [CrossRef]
8. Liu, Y.; Li, P.; Chen, H.; Yang, J.; Ren, X. A Big Area Ratio Liquid Rocket Engine Nozzle with Full-Flow in Low Altitude. *J. Propuls. Technol.* **2022**, *43*, 205–212.
9. Yu, K.; Chen, Y.; Huang, S.; Xu, J. Inverse Design Method on Scramjet Nozzles Based on Maximum Thrust Theory. *Acta Astronaut.* **2020**, *166*, 162–171. [CrossRef]
10. Yu, K.; Chen, Y.; Huang, S.; Xu, J. Inverse Design Method on Scramjet Nozzle with Full Geometrical Constraints for Nozzle-Afterbody Integration. *J. Aerosp. Eng.* **2021**, *34*, 04021004. [CrossRef]
11. Wang, Z.; Liu, A.; Cai, Y. Design method and flow field simulation of single expansion ramp nozzle. *Gas Turbine Exp. Res.* **2007**, *20*, 8–12.
12. Argrow, B.M.; Emanuel, G. Comparison of minimum length nozzles. *J. Fluids Eng.* **1988**, *110*, 283–288. [CrossRef]
13. Shyne, R.; Keith, T., Jr. Analysis and design of optimized truncated scarfed nozzles subject to external flow effects. In Proceedings of the 26th Joint Propulsion Conference, Orlando, FL, USA, 16–18 July 1990.
14. Hoffman, J.D. Design of compressed truncated perfect nozzles. *AIAA Pap.* **2015**, *3*, 150–156.
15. Lan, Q. The Method of Characteristics for the Inverse Problem of Three-Dimensional Hypersonic Aerodynamics. Master's Thesis, National University of Defense Technology, Changsha, China, 2017.
16. Liu, H.; Zhao, Y. Aerodynamic Inverse Design via Characteristics Tracing. *J. Propuls. Technol.* **2017**, *38*, 289–297.
17. Bare, E.A.; Capone, F.J. *Static Internal Performance of Convergent Single-Expansion-Ramp Nozzles with Various Combinations of Internal Geometric Parameters*; NASA: Washington, DC, USA, 1989.
18. Zucrow, M.J.; Hoffman, J.D. *Gas Dynamics*; vol. 2–Multidimensional Flow; John Wiley & Sons, Inc.: New York, NY, USA, 1977.
19. Mo, J.; Xu, J.; Quan, Z.; Yu, K.; Lv, Z. Design and cold flow test of a scramjet nozzle with nonuniform inflow. *Acta Astronaut.* **2015**, *108*, 92–105. [CrossRef]